J. Fluid Mech. (2000), *vol.* 415, *pp.* 89–116. Printed in the United Kingdom

Numerical study of internal wave–caustic and internal wave–shear interactions in a stratified fluid

By A. JAVAM[1], J. IMBERGER[2] AND S. W. ARMFIELD[1]

[1] Department of Mechanical Engineering, University of Sydney, Sydney, 2006, Australia

[2] Department of Environmental Engineering, Centre for Water Research, University of Western Australia

(Received 6 June 1996 and in revised form 25 February 2000)

The behaviour of internal waves at a caustic level, turning point and critical layer have been investigated numerically. At a caustic reflection, a triad interaction was formed within the reflection region and the internal wave energy was transferred to lower frequencies (subharmonics). This resulted in a local subharmonic instability. One of the excited internal waves penetrated the caustic level and propagated downwards. This downward propagating wave then produced a second caustic where further reflection could take place. At a turning point, nonlinear interaction between the incident and reflected waves transferred energy to higher frequencies (evanescent trapped waves) which resulted in a superharmonic instability. At the critical level, energy was transferred to the mean flow. As the degree of nonlinearity increased, more energy was found to be transferred and overturning resulted due to a shear instability.

1. Introduction

The breaking of internal waves is of importance for the mixing in stratified lakes, estuaries and oceans. There are many ways in which internal waves break. These include shear instability (Woods 1968; Thorpe 1968*a*, 1978), formation of rotors (Davis & Acrivos 1967; Miranda & James 1992), static instability (Thorpe 1968*b*, 1981), critical layer absorption (Lin *et al.* 1993), parametric instability (McEwan & Robinson 1975; Drazin 1977; Bouruet-Aubertot, Sommeria & Staquet 1995), convective instability (Orlanski & Bryan 1969; Delisi & Orlanski 1975) and superharmonic instability (Javam, Armfield & Imberger 2000; Teoh, Ivey & Imberger 1997) (see Thorpe 1994 for a review). In this paper, convective instabilities at caustic reflections, shear instabilities at critical layers and superharmonic instabilities at turning points are investigated.

1.1. *Wave–caustic interaction*

In convective instabilities, which occur at caustic reflections (Orlanski & Bryan 1969), breaking develops from existing large-amplitude internal waves as the isopycnal slopes increase; particles at the wave crest are advected forward relative to the trough, leading to a local density inversion with the potential for a Rayleigh–Taylor instability. Convective instabilities can take place in the absence of ambient shear, although they are often augmented by shear (Thorpe 1978; Munk 1980).

Orlanski & Bryan (1969) (see also Munk 1980) derived the required critical amplitude for a convective instability to occur in the ocean and verified their analysis with numerical experiments. Based on the following simple argument Orlanski & Bryan (1969) concluded that, in the ocean, conditions favoured convective instabilities over shear instabilities. According to linear theory, the vertical wavenumber of a progressive internal wave in an unbounded continuously stratified fluid is given by the dispersion relation:

$$k_y = k_x \left(\frac{N^2 - \omega^2}{\omega^2} \right)^{1/2}, \tag{1.1}$$

and in the limit $\omega \ll N$, this equation reduces to

$$k_y = \frac{k_x N}{\omega}, \tag{1.2}$$

where k_x and k_y are the horizontal and vertical wavenumbers, ω is the wave frequency and N is the buoyancy frequency. From equation (1.2) it follows that

$$\frac{k_y u}{N} = \frac{u}{\omega/k_x}, \tag{1.3}$$

where u is the particle velocity of the wave. For a wave to suffer a shear instability $k_y u/N = 1/\sqrt{Ri} > 2$, but a convective instability will occur when $u/(\omega/k_x) > 1$; consequently, convective instabilities are likely to occur first.

A momentum source oscillating with a frequency ω in a density-stratified fluid, with a buoyancy frequency N, will produce a cross-wave pattern with four beams of energy, inclined at angles of $\theta = \sin(\omega/N)$ to the horizontal (Mowbray & Rarity 1967; Javam *et al.* 2000). When the buoyancy frequency varies with height and there is no mean flow, the beams are curved and reflections occur at a level where $N = \omega$ (see Phillips 1977). Such levels will be referred to as caustics in the present paper. At a caustic the vertical component of the wavenumber vector and the group velocity vanish and the wave energy is reflected. The incident and reflected wave trains have the same frequency, but opposite horizontal wavenumbers. The superposition of these two waves, travelling in the opposite direction, constitutes a standing wave mode in the interaction region (Phillips 1977).

By formulating the problem near the caustic in terms of the Airy function and with the use of ray theory, Lighthill (1978) was able to show that internal waves were reflected at caustics with their amplitude unchanged, but with a phase shift of $\pi/2$. Lighthill's results were used by Liu, Nicolaou & Stevenson (1990) and Nicolaou, Liu & Stevenson (1993) to show that, for a linear shear, the phase shift remains $\pi/2$, similar to that in a fluid at rest.

The first goal of the present paper was to investigate the reflection of the internal waves at the caustic in detail and to show that overturning can occur in the reflection region. A triad interaction was found to form and energy was transferred to lower frequencies, eventually leading to subharmonic instabilities and turbulent kinetic energy dissipation. The latter is, however, poorly modelled with the present scheme.

1.2. *Wave–shear interaction*

1.2.1. *Turning point*

Internal wave–shear interaction in a fluid with constant buoyancy frequency and sheared mean flow has been a topic of much interest since the effect of critical layers was demonstrated by Miles (1961). For waves propagating in the same direction as

a current with shear, a level, y_c, exists where the mean velocity $U(y_c)$ of the current equals the horizontal phase velocity c_p of the internal waves. For waves propagating against the current, a point, y_t, exists where the buoyancy frequency N is equal to the relative wave frequency $\omega - U(y_t)k_x$, where k_x is the horizontal wavenumber. Such locations will be referred to as critical level and turning point, respectively, in the present paper. At the turning point, the rays become horizontal. Phillips (1977) formulated a WKB solution in the neighbourhood of the turning point, in terms of the Airy function, and showed that within this approximation, total reflection occurred at the turning point, similar to that which occurs at a caustic. Internal wave reflection at turning points has otherwise received little attention.

Our second goal was to show that internal wave–shear interaction becomes unstable at the turning point where the energy is transferred to higher modes which subsequently leads to internal waves overturning through a superharmonic instability.

1.2.2. *Critical layer absorption*

As the ray approaches the critical level it curves so that the vertical wavenumber becomes much greater than the horizontal wavenumber and the group velocity becomes nearly horizontal. Thus, the wave packet is neither transmitted nor reflected and simply slows down, relative to the flow, until either viscosity or nonlinearities destroy it as a coherent entity (Bretherton 1969); the waves are then absorbed and give their energy to the mean flow, causing a local acceleration of the flow (Phillips 1977). This transfer of momentum flux from the wave to the mean flow is commonly known as critical layer absorption.

The first detailed studies of critical layer absorption were conducted by Bretherton (1966) and Booker & Bretherton (1967). Their linear unsteady inviscid and initial value analysis revealed that for local Richardson numbers $N^2/(\mathrm{d}U/\mathrm{d}y)^2$ of order unity or greater, the critical layer represented a nearly impenetrable barrier to incoming waves with a reduction of wave amplitude of $O(\exp[-2\pi(Ri - 1/4)^2])$. Thus, for $Ri > 1/4$, the critical level acts effectively as a complete absorber. Hartman's (1975) linear analysis showed that as the Richardson number approached 1/4, the group velocity of the wave packet decreased to zero near the critical layer while the vertical displacement remained finite. Thorpe (1981) and Koop (1981) using laboratory experiments in parameter ranges conducive to instability showed that critical layer instabilities were convective instabilities. This was confirmed by Fritts (1982) using numerical simulations. However, Koop & McGee (1986) observed both Kelvin–Helmholtz and convective instabilities in their experiments and Winters & D'Asaro (1989) also suggested that the instabilities at the critical layer are of a shear instability nature, although the numerical resolution used by these authors was insufficient to allow definitive conclusions to be drawn. The uncertainty about the nature of the instability at a critical layer motivated Lin *et al.* (1993) to study two-dimensional interaction of internal waves and shear at critical layers with the goal of determining the nature of the instabilities. They concluded that as a wave packet approached a critical layer, part of the energy is transferred to the mean flow and the remainder is focused into increasingly thin regions. Strong shear and unstable density gradients arise as the layer thins leading to a shear instability; however, unstable density profiles occurred much earlier, so once again the conclusions were not clear. Therefore, our third goal was to investigate the mechanism of instability near the critical layer in order to clarify the above ambiguities.

2. Model formulation

Two-dimensional motion of an incompressible and viscous fluid is governed by the equations of conservation of momentum, mass and volume. Employing the Boussinesq approximation, these equations, in non-dimensional form, are

$$\frac{\partial u}{\partial t} + Ke\left[u\frac{\partial u}{\partial x} + v\frac{\partial u}{\partial y}\right] = -\frac{\partial p}{\partial x} + Re^{-1}\nabla^2 u, \tag{2.1}$$

$$\frac{\partial v}{\partial t} + Ke\left[u\frac{\partial v}{\partial x} + v\frac{\partial v}{\partial y}\right] = -\frac{\partial p}{\partial y} - \rho + Re^{-1}\nabla^2 v + f(x,y)\sin(t), \tag{2.2}$$

$$\frac{\partial \rho}{\partial t} + Ke\left[u\frac{\partial \rho}{\partial x} + v\frac{\partial \rho}{\partial y}\right] = Ri_m\, g(y)^2\, v + Re^{-1}Pr^{-1}\nabla^2\rho, \tag{2.3}$$

$$\frac{\partial u}{\partial x} + \frac{\partial v}{\partial y} = 0, \tag{2.4}$$

where

$$\left.\begin{aligned} Ri_m &= \frac{(-g/\rho_o)(\mathrm{d}\hat{\rho}/\mathrm{d}y|_{y_m})}{\omega^2} = \left[\frac{N_m}{\omega}\right]^2, \quad Ke = \frac{Fk_x}{\omega^2}, \\ Pr &= \frac{v}{\kappa}, \quad Re = \frac{\omega}{k_x^2 v}, \quad \nabla^2 = \frac{\partial^2}{\partial x^2} + \frac{\partial^2}{\partial y^2}, \end{aligned}\right\} \tag{2.5}$$

and where $N_m = ((g/\rho_o)|\mathrm{d}\hat{\rho}/\mathrm{d}y|_{y_m})^{1/2}$ is the buoyancy frequency at the level of the momentum source y_m, $g(y)$ is a function used to define the buoyancy frequency profile for the nonlinear stratification, $N = N_m g(y)$, t is the time, $\rho, \hat{\rho}$ and ρ_o are the fluctuating, background and reference densities respectively, v is the coefficient of kinematic viscosity, κ is the coefficient of thermal diffusivity. Details of the non-dimensionalization are given in Javam *et al.* (2000). The momentum source $f(x,y)\sin t$ is used to generate internal wave beams, ω is the frequency of the momentum sources, $f(x,y)$ is the non-dimensional localization function, and F is the amplitude of the momentum source. The Keulegan number Ke represents the ratio of the period of oscillation to the time taken for an eddy to roll up. Therefore, for large Keulegan numbers the period of oscillation is large compared to the time taken for eddies to roll up, implying the importance of the advective acceleration terms. By contrast, the Reynolds number is the ratio of the time scales: $1/k_x^2 v$ and ω^{-1}.

The localization function $f(x,y)$ is defined by

$$f(x,y) = \begin{cases} \cos(x - X_l)\exp(-300|y - Y_l|^3) & \text{if } |x - X_l| \leqslant 3\pi/2 \\ 0 & \text{otherwise,} \end{cases} \tag{2.6}$$

in which X_l and Y_l are the horizontal and vertical non-dimensional locations of the momentum source respectively.

A finite-volume method is used to solve the full Navier–Stokes equations based on the model developed by Armfield (1994). The method was extended for (i) generation of internal waves using a momentum source in a stratified fluid, and (ii) open boundaries; details are given in Javam *et al.* (2000).

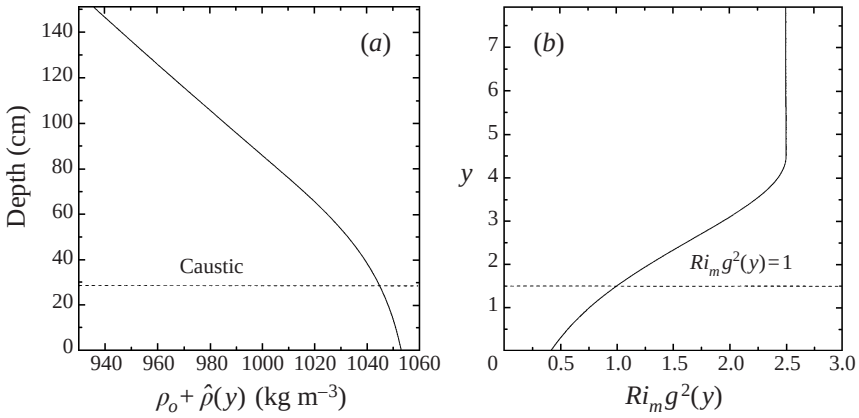

FIGURE 1. (*a*) Density and (*b*) model Richardson number distribution.

3. Results

3.1. *Caustic reflections*

3.1.1. *Reflection coefficient at caustic reflections*

At a level where the buoyancy frequency becomes equal to the imposed frequency, or in non-dimensional form when locally $Ri_m g(y)^2 = 1$, internal waves are reflected internally. The characteristics of the reflection process at a caustic depend on the values of the Keulegan and Reynolds numbers. To investigate this dependence a nonlinear stratification with a buoyancy frequency distribution of $N(y) = N_m g(y)$ was used in the simulations, with

$$g(y) = \begin{cases} 1/\cos h\,[a(y - y_m)] & \text{if } y \leqslant y_m \\ N_m & \text{if } y > y_m, \end{cases} \tag{3.1}$$

where a controls the location of the caustic. Figures 1(*a*) and 1(*b*) depict $\rho_o + \hat{\rho}$ and $Ri_m g(y)^2$ as a function of y. To explore the effect of viscosity and nonlinearity, simulations were performed using different Keulegan and Reynolds numbers for a computational domain of 198×132 uniform cells with non-dimensional size of $\Delta x = \Delta y = 0.12\pi$ and a time step of $\Delta t = 2\pi/1000$; the momentum source, having an extent of one and a half wavelengths, was placed 10 cells above the centre in the computational domain. First, the Reynolds number was kept at $Re = 1600$ and the following Keulegan numbers were used: $Ke = 0.0125, 0.025, 0.05$ and 0.1. The Keulegan number was then kept at $Ke = 0.0125$ and the following Reynolds numbers were used: $Re = 25\,000, 10\,000, 4000$ and 1600.

As discussed before, for an internal wave propagating in a fluid at rest, the linear and inviscid solutions predict a phase shift of $\pi/2$ (Lighthill 1978; Liu 1989). Referring to figure 2, let the x'-direction be perpendicular to the centreline of the lower right cross-arm pointing in the direction of the phase velocity vector. It follows that it is directed upwards before reflection and downwards after reflection. The waveforms of the cross-arm and its reflection are shown in figures 3(*a*) to 3(*g*). In these plots the origin of the x'-axis corresponds to the position at which the maximum amplitude of the incident wave occurs. These plots indicate that the reflection, at the centre of the wave beam, leads the cross-arm in time by approximately $\pi/2$.

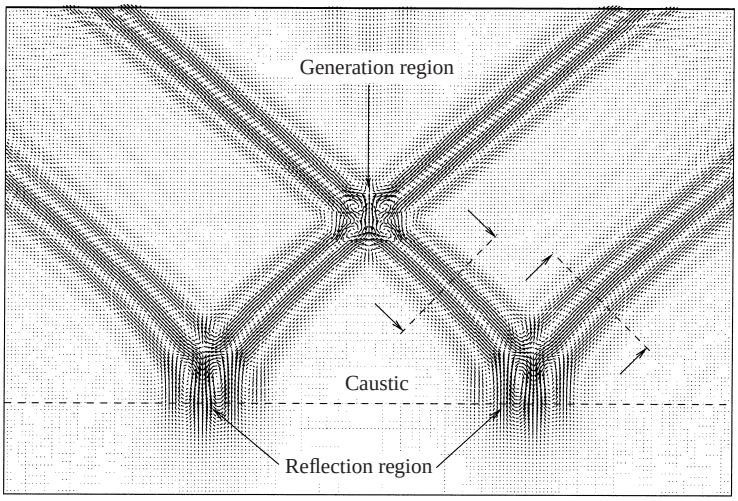

FIGURE 2. Velocity vector plot for the internal wave reflection at $T = 20$; $Ke = 0.1$, $Ri_m = 2.5$, $Re = 23\,000$, and $Pr = 7$.

Re	Ke	Incident energy flux density $\sum p_i u_i$	Reflected energy flux density $\sum p_r u_r$	Reflection coefficient C_r
1600	0.1	0.1225	0.0269	0.220
1600	0.05	0.1117	0.0274	0.245
1600	0.025	0.1100	0.0297	0.270
1600	0.0125	0.1034	0.3050	0.295
4000	0.0125	0.1637	0.0753	0.460
10 000	0.0125	0.2014	0.1259	0.625
25 000	0.0125	0.2389	0.1887	0.790

TABLE 1. Reflection coefficients for different Keulegan and Reynolds numbers.

The reflection coefficient C_r, defined as

$$C_r = \frac{\int^{Raywidth} p_r q_r \mathrm{d}\lambda}{\int^{Raywidth} p_i q_i \mathrm{d}\lambda}, \tag{3.2}$$

is the ratio between the energy flux density of the reflected waves and the incident waves. Here p_i and q_i are the pressure and velocity along the incident ray and p_r and q_r are the pressure and velocity along the reflected ray. The results from a number of simulations with varying values of Ke and Re are shown in table 1 and the variation with Reynolds number is plotted in figure 4; the reflection coefficient clearly increases with increasing Reynolds number, approaching the linear result of perfect reflection.

3.1.2. *Wave overturning at caustic reflections*

The above discussion showed that as Ke increased the reflection coefficient decreased and more energy was trapped within the reflection region. In this section we will demonstrate that nonlinear advection can cause overturning at the reflection

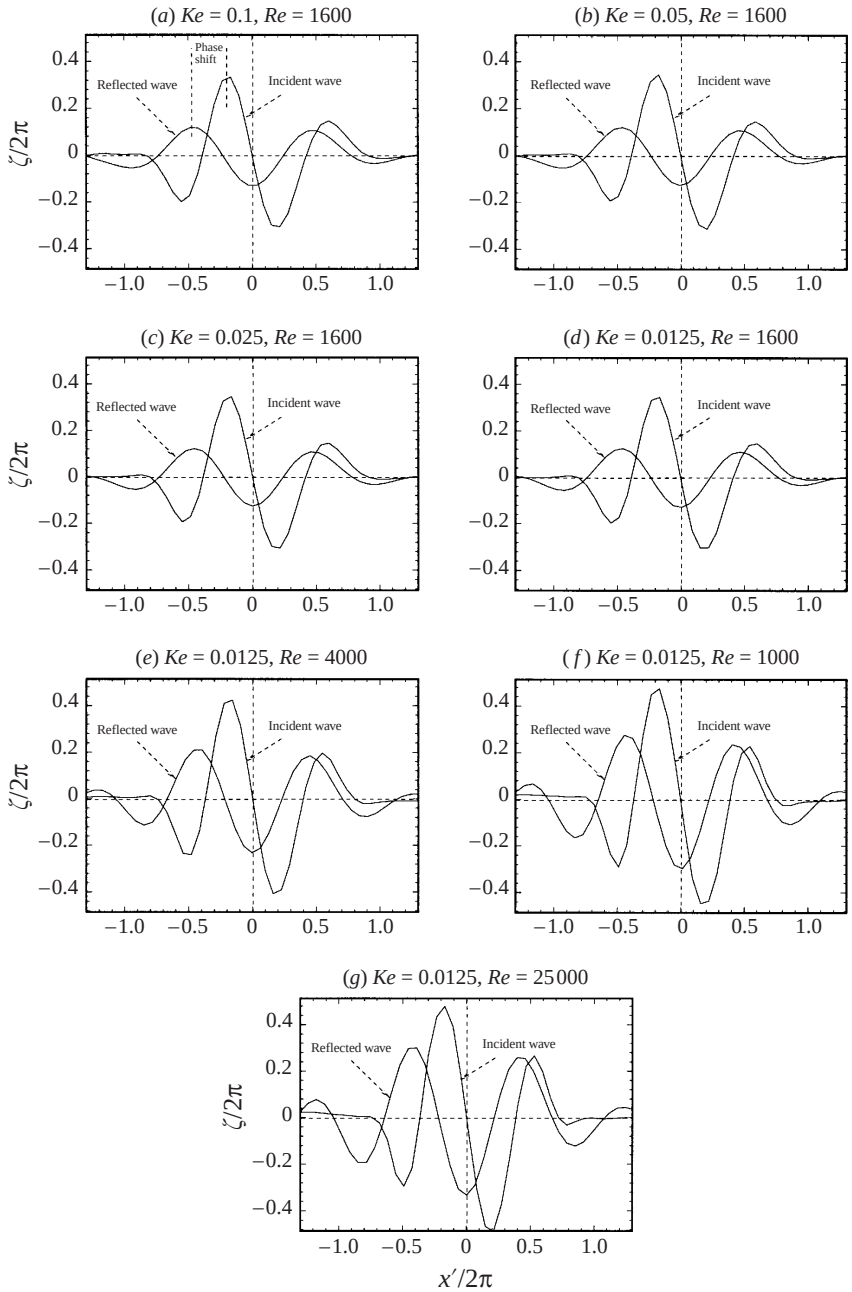

FIGURE 3. The waveforms of the internal wave before and after the reflection. The origin of the x'-axis corresponds to the position at which the maximum amplitude of the incident wave occurs and the group velocity is pointing in the direction of increasing y'. At the centre of the wave beam, a phase shift of $\pi/2$ occurs when internal waves reflect.

regions and we will also explore the mechanism of instability in this region. In order to investigate the nonlinear advection, the non-dimensional parameters were chosen as follows: $Pr = 7, Ri_m = 2.5, Re = 23\,000$, and $Ke = 0.1, 0.2, 0.3, 0.35$ and 0.4.

The velocity vector plot for the low-Ke case (0.1) is shown in figure 2 at $T = 20$,

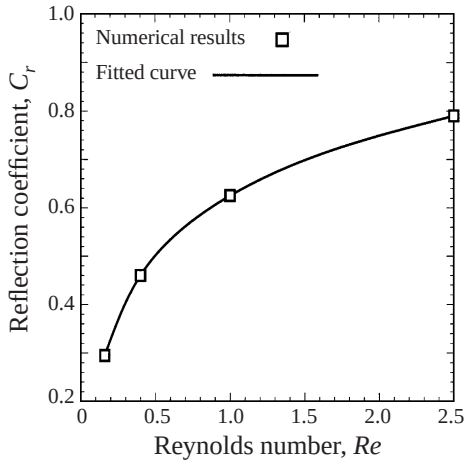

FIGURE 4. Reflection coefficient plot for the different Reynolds numbers at $Ke = 0.0125$. The reflection coefficient increases with increasing Reynolds number.

where the time T is in wave periods ($T = t/2\pi$). The incident waves were reflected almost perfectly and the flow field exhibited all the features of the linear Airy function solution derived by Lighthill (1978). On increasing the Keulegan number beyond 0.1, nonlinear effects changed the basic flow field in the region of reflection, resulting in smaller-scale motions as illustrated in figure 5. For sufficiently large incident amplitude, a local gravitational instability appeared in the flow. Figure 6 contains density contour plots from simulations with different Keulegan numbers at the first indication of overturning. For $Ke = 0.1$ (figures 2 and 6), the wave amplitude did not increase in the reflection region and overturning did not occur even after a simulation time of 20 wave periods. As seen in figure 6 overturning did, however, occur once $Ke \geqslant 0.2$ and overturning occurred faster after initiation of the disturbance with increasing Ke. The local properties for the cases with $Ke > 0.1$ were all similar, so the results from $Ke = 0.35$ were chosen as a focus for discussion.

Stages of the overturning process for this case are displayed in figure 7. It is seen that the overturned regions remained at the same vertical level, but moved horizontally with the trough of the waves. Further, the overturned region appeared to become horizontally elongated with time, with a second region forming as the second trough entered the region and subsequently steepened. The nature of the instabilities which occurred in the reflection region may be clarified by looking at the frequency content of the oscillations. The forcing frequency was unity, but the short-time spectral analysis shown in figure 8, with $\Delta T = 2\pi/1000$, indicates that oscillations with a frequency of 0.3 (at locations C and E) and 0.7 (at locations D and E) were excited. Locations are shown in figure 5. The wave with the frequency of 0.7 penetrated the caustic level and emerged below, propagating downwards to possibly a new caustic level. By contrast the low-frequency wave (0.3) propagated upwards at a more shallow angle than the incident wave. Both these features are also evident in figure 8, and plate 2 in Delisi & Orlanski (1975). Comparisons between figure 2 and figure 5 show these secondary waves only occurred at larger values of Ke.

Orlanski & Bryan (1969) have shown that, for locally unstable density gradients to appear, the horizontal advection must balance the local time rate of change of density. This is true for a single wave when the horizontal velocity u equals or exceeds the horizontal phase velocity. The time variation of horizontal velocities

(*a*)

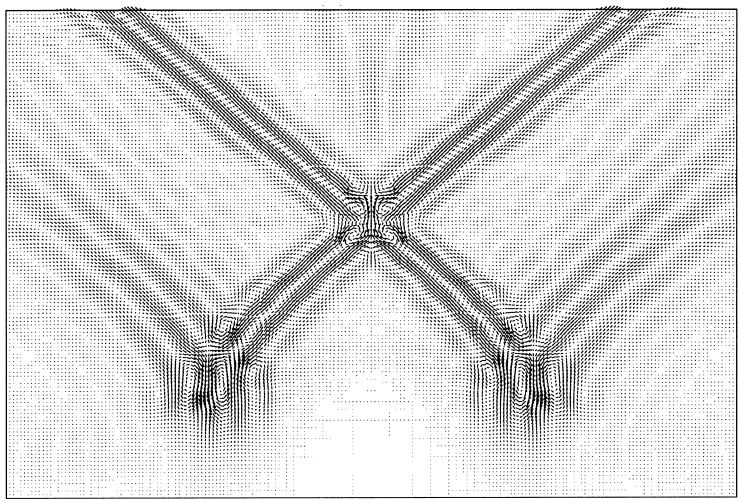

(*b*)

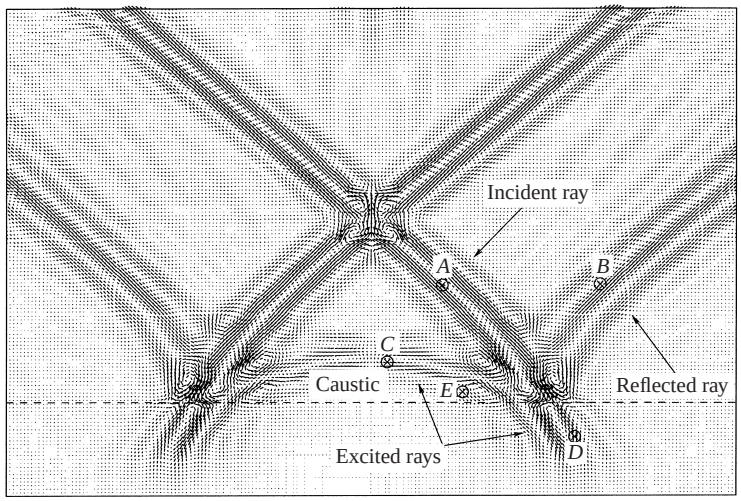

FIGURE 5. Velocity vector plots at (*a*) $T = 12$ and (*b*) $T = 18$ for the internal wave reflection; $Ke = 0.2$, $Ri_m = 2.5$, $Re = 23\,000$, and $Pr = 7$. Lower modes develop with an increasing Keulegan number.

within the excited rays in which the overturning occurred and the horizontal phase speed for those modes are shown in figure 9, where it is seen that the horizontal velocity exceeded the horizontal phase velocity immediately before overturning took place. Since the wave energy is propagated along the rays, the overturned region was stretched out along lines that were at an angle to the horizontal equal to the angle which the excited rays made to the horizontal (figure 7).

In the reflection region there exist, therefore, a number of waves concurrently. A sequence of two-dimensional wavenumber spectra (figure 10) for the density fluctuation within the interaction region for different times shows this clearly. Higher wavenumbers appeared as soon as the reflected and incident waves began to interact

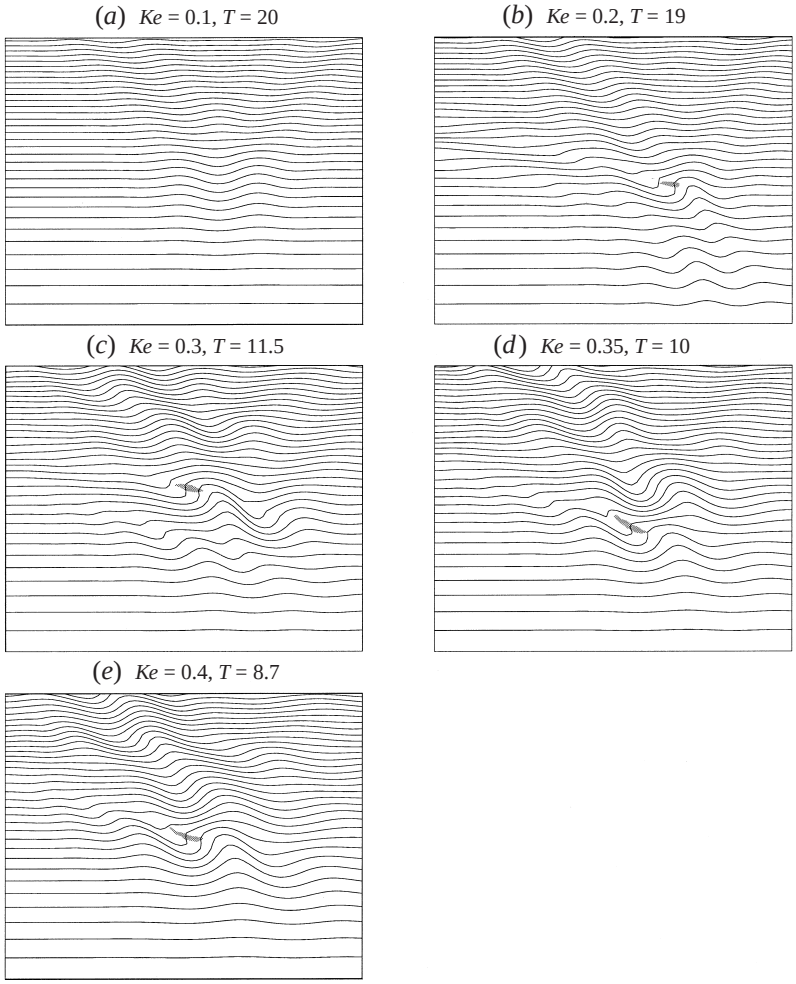

FIGURE 6. Density contour plots for various Keulegan numbers; $Ri_m = 2.5$, $Re = 23\,000$, and $Pr = 7$. Shading indicates regions of density overturning. The location of the caustic is at the central level of these plots. By increasing the Keulegan number, the nonlinear effects change the basic flow field in the region of reflection. The time at which the first overturning for the different Ke occurs is shown at the top of each plot (*b–e*). It is also evident that for the larger Ke the overturning occurs earlier.

spatially (figure 10; $T = 4$), while overturning first occurred at $T = 10$ (figure 6*d*). The following wavenumbers were present immediately before overturning:

$$K_1 = (-6/2\pi, -22.5/2\pi); \qquad K_2 = (18/2\pi, 15/2\pi); \qquad K_3 = (12/2\pi, -7.5/2\pi).$$

This wavevector configuration is shown in figure 11 and satisfies the weak interaction criterion:

$$\Delta K = K_1 + K_2 - K_3 = 0, \quad \omega_1 + \omega_2 - \omega_3 = 0, \tag{3.3}$$

where

$$K_i = (k_x, k_y, k_z)_i.$$

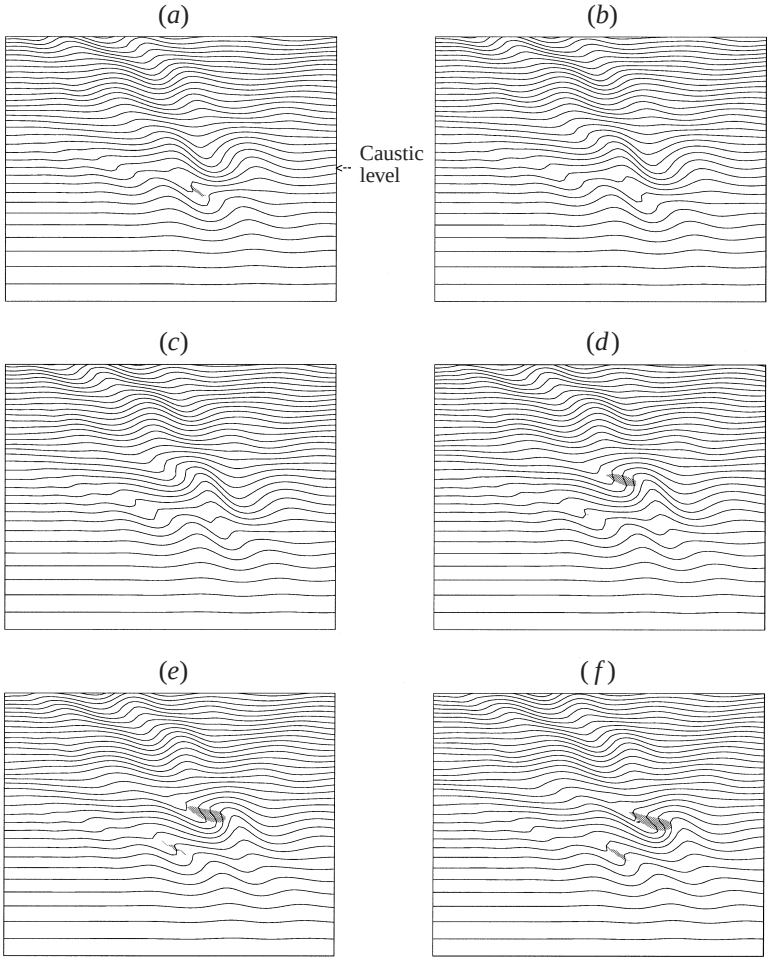

FIGURE 7. Density contour plots; $Ke = 0.35$, $Ri_m = 2.5$, $Re = 23\,000$, and $Pr = 7$. Shading indicates regions of density overturning. Times are (*a*) 10.2, (*b*) 10.4, (*c*) 10.6, (*d*) 10.8, (*e*) 11 and (*f*) 11.2. The location of the caustic is at the central level of these plots. The overturning occurs along lines that lie at an angle to the horizontal, which is equal to the angle which the lower mode rays make to the horizontal.

Therefore, the reflected and incident waves interacted first spatially, then the nonlinear effects excited a nonlinear resonant triad interaction. The energy was transferred to lower modes and the amplitude of the lower modes increased until the horizontal advection of isopycnals caused overturning.

3.2. *Turning point*

For this part of the study, the simulation domain, of non-dimensional size $14.4\pi \times 23.76\pi$, consisted of uniform cells with non-dimensional size of $\Delta x = \Delta y = 0.12\pi$. The unperturbed flow was linearly stratified and had a hyperbolic velocity profile:

$$U(y) = 2c_p/\cosh(b(y - 0.84)^2), \tag{3.4}$$

where c_p is the phase velocity of the generated internal wave and the parameter b controls the slope of the initial mean velocity profile (see figure 12). Apart from the

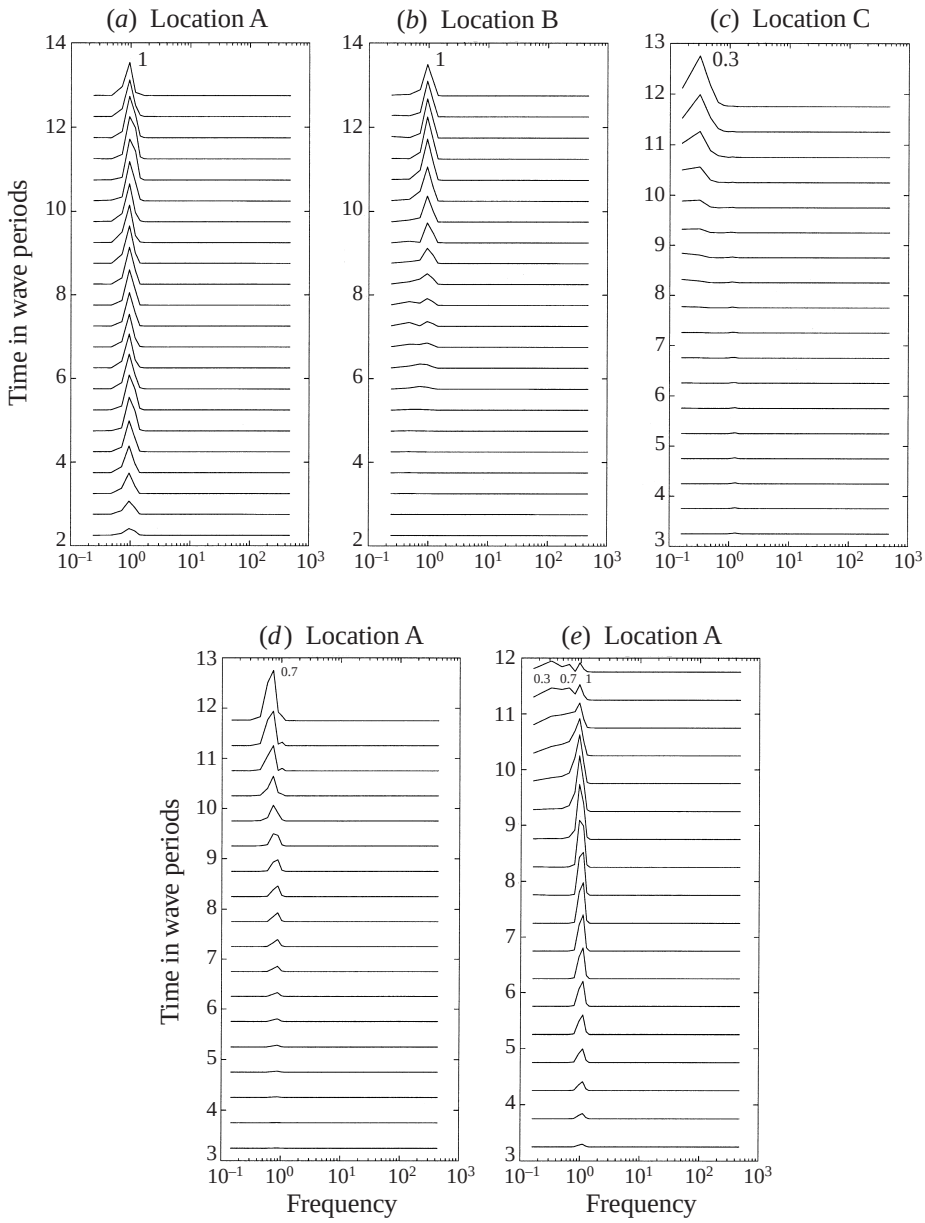

FIGURE 8. Short-time Fourier distribution for density fluctuations; $Ke = 0.35$, $Ri_m = 2.5$, $Re = 23\,000$, and $Pr = 7$, showing the generation of lower modes. Locations shown on figure 5.

model Richardson number Ri_m, two more definitions of Richardson number were used. The first, denoted Ri_b, is a Richardson number based upon the initial mean flow and background stratification and the second, Ri_l, is based upon the total velocity and density profiles. These definitions are

$$Ri_b = \frac{\frac{g}{\rho_o}\frac{\mathrm{d}\hat{\rho}}{\mathrm{d}y}}{(\mathrm{d}U/\mathrm{d}y)^2}, \quad Ri_l = \frac{\frac{g}{\rho_o}\frac{\mathrm{d}(\hat{\rho}+\rho)}{\mathrm{d}y}}{(\mathrm{d}u/\mathrm{d}y)^2}. \tag{3.5}$$

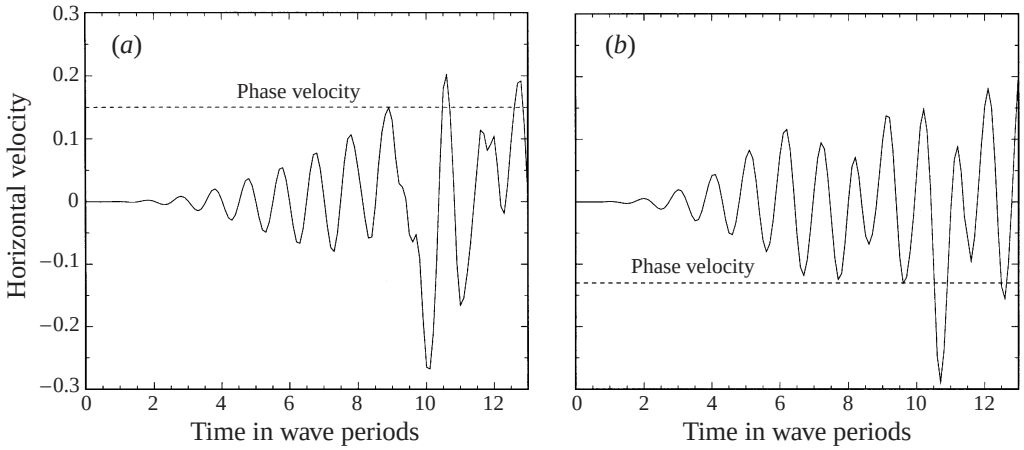

FIGURE 9. Time variation of horizontal velocity within the overturning region; $Ke = 0.35$, $Ri_m = 2.5$, $Re = 23\,000$, and $Pr = 7$. The horizontal velocity exceeds the phase velocity immediately before the overturning: (*a*) lower mode with a frequency of 0.3, (*b*) lower mode with a frequency of 0.7.

A momentum source, having an extent of one and a half non-dimensional wavelengths, was placed 10 cells above the centre in the computational domain.

In order to investigate the influence of nonlinearity on the reflection of internal waves at a turning point, a series of simulations was performed for increasing Keulegan numbers, while the other parameters were kept constant at the values: $Re = 23\,000, Ri_m = 2.5, Ri_b(y_c) = 40$ and $Pr = 7$.

At the turning point, the vertical wavenumber reduced dramatically. It did not, however, approach zero for the lower Keulegan number case $Ke = 0.1$. The incident wave continued propagating with a low vertical wavenumber until the shear changed sign and the vertical wavenumber started to increase (figure 13*a*).

The ray paths in a shear flow can be obtained by (Liu *et al.* 1990)

$$\frac{\mathrm{d}x}{\mathrm{d}y} = (1 - \sin^2\theta)^{1/2} + \left(\frac{Uk_x}{N}\right)\left(\frac{1}{\sin^2\theta(1 - \sin^2\theta)^{1/2}}\right) \tag{3.6}$$

in which the dispersion relationship is

$$\sin^2\theta = (\omega - k_x U)^2/N^2, \tag{3.7}$$

where θ is the angle to the vertical of the group velocity relative to the fluid. Reflection occurs at a caustic (quiescent fluid with nonlinear stratification where $\omega = N(y_r)$) and also occurs at a turning point (shear flow where $\omega - k_x U(y) = N(y_r)$). At the reflection point ($y = y_c$), $\sin^2\theta$ is unity. Therefore, near the reflection point ($y \sim y_c$) the dispersion relationship can be approximated as

$$\sin^2\theta \sim 1 - \beta(y - y_r), \tag{3.8}$$

so that, near the caustic, $U = 0$, (3.6) becomes

$$\frac{\mathrm{d}x}{\mathrm{d}y} \sim \beta^{1/2}(y - y_r)^{1/2},$$

which implies

$$(y - y_r) \sim Ax^{2/3}. \tag{3.9}$$

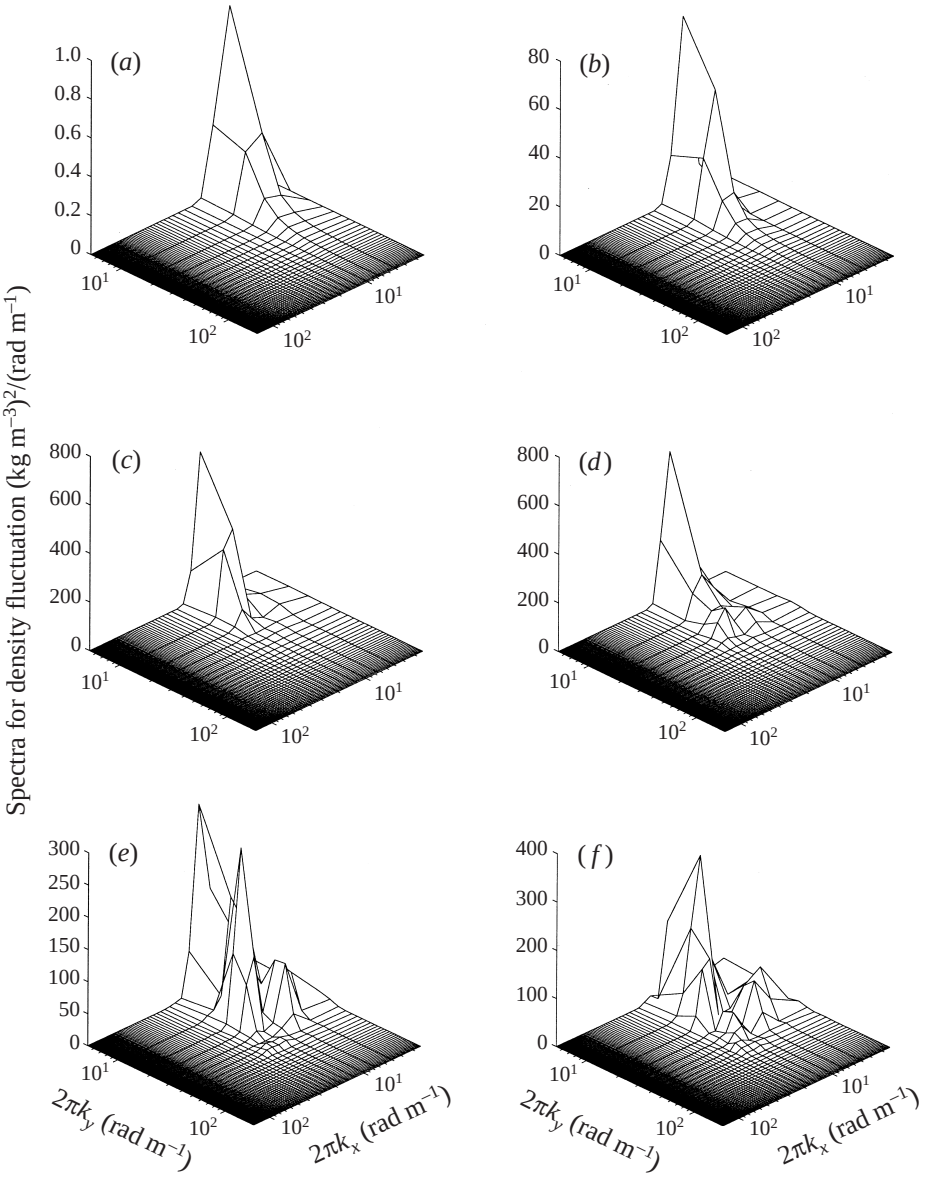

FIGURE 10. Two-dimensional wave number spectrum for the reflection region; $Ke = 0.35$, $Ri_m = 2.5$, $Re = 23\,000$, and $Pr = 7$. Times are (*a*) 2, (*b*) 4, (*c*) 8, (*d*) 10, (*e*) 11, and (*f*) 12. Higher wavenumbers appear as soon as the reflected and incident waves begin to interact spatially. For this case, the overturning occurs at $T = 10.0$ (figure 6).

While near the turning point (3.6) and (3.8) lead to

$$\frac{\mathrm{d}x}{\mathrm{d}y} \sim \beta^{1/2}(y - y_r)^{1/2} + \frac{U(y)k_x}{N(y)} \frac{1}{(1 - \beta(y - y_r))\beta^{1/2}(y - y_r)^{1/2}}.$$

Since $(y - y_r)$ is very small, the second term dominates and $1 - \beta(y - y_r) \sim 1$ so we obtain

$$\frac{\mathrm{d}x}{\mathrm{d}y} \sim \frac{U(y)k_x}{N(y)} \beta^{-1/2}(y - y_r)^{-1/2},$$

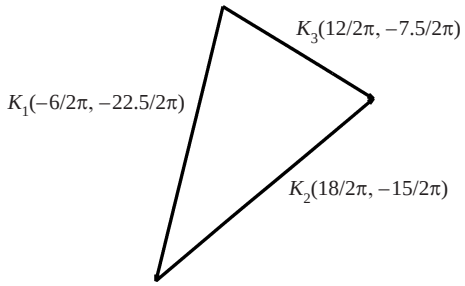

FIGURE 11. Wavevector configuration observed immediately before overturning: $K_1 = K_2 + K_3$ at $T = 10$, $Ke = 0.35$, $Ri_m = 2.5$, $Re = 23\,000$, and $Pr = 7$.

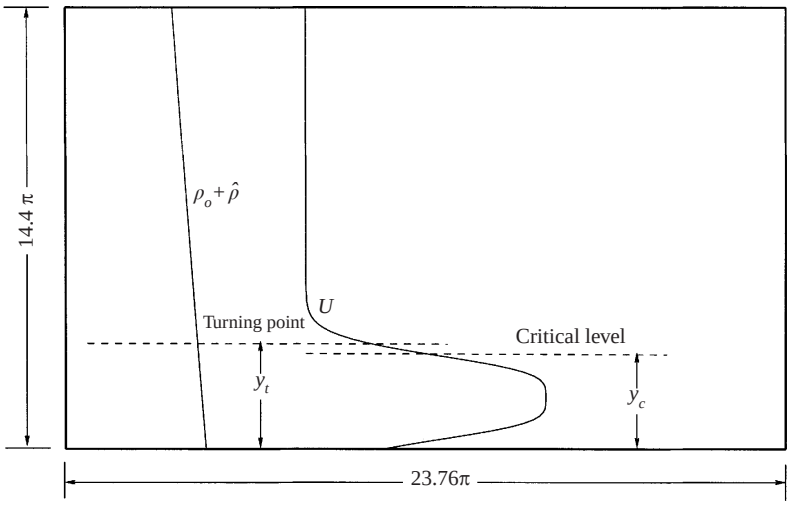

FIGURE 12. Initial configuration; the computational domain is a $14.4\pi \times 23.76\pi$ box. The background stratification is linear and the initial mean velocity has a hyperbolic profile.

implying

$$(y - y_r) \sim Bx^2. \tag{3.10}$$

Equations (3.9) and (3.10) are plotted in figure 14. As mentioned in Liu *et al.* (1990) and Nicolaou *et al.* (1993) and as anticipated by Lighthill (1978) and Hartman (1975), shown in this figure and demonstrated by the velocity vector plots in figures 2 and 13(*c*), the tangents to the rays are vertical at the caustics and horizontal at the turning points. It has been suggested in the literature (e.g. Koop 1981) that the tangents to the rays are also vertical at the turning points; however this was not observed here.

Figures 15 and 16 contain a series of plots depicting the evolution of the wave reflection with time at the turning point, for the case $Ke = 0.3$. The velocity field is indicated by vectors, the density field by contour lines, and shading is used to indicate shear unstable regions (i.e. where $Ri_l < 1/4$). The plots indicate that the amplitude of the wave increased with time until the wave reached a sufficiently large amplitude at $T = 10.8$ when density overturning occurred. Figures 16(*a*) and 16(*b*) show that the unstable region propagated against the mean current. The amplitude of the density field below the turning point did not change during the simulation, demonstrating that there was a constant transmission of the wave energy past the turning point.

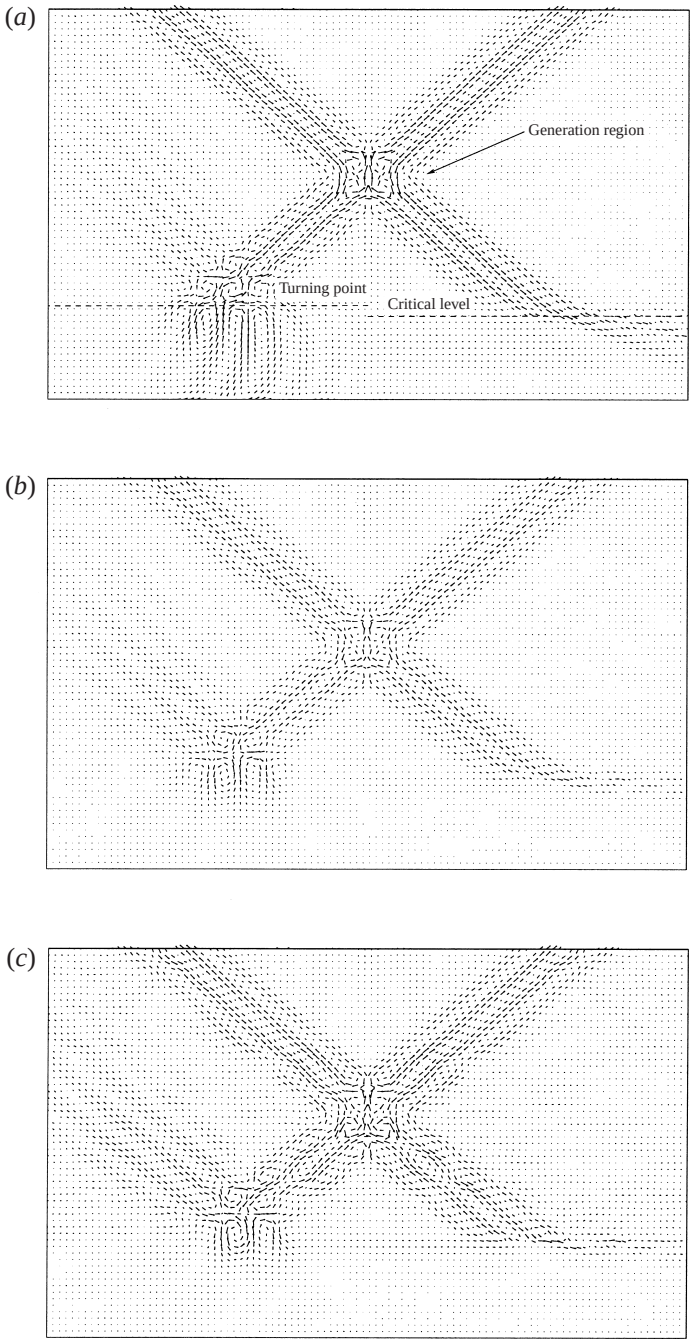

FIGURE 13. Velocity vector plots. Keulegan numbers are: (*a*) 0.1 ($T = 12$), (*b*) 0.2 ($T = 10$), and (*c*) 0.3 ($T = 8$). At high Keulegan numbers the incident waves cannot propagate beyond the critical level and turning point.

The small spatial scales were formed as soon as the internal wave beam reached the turning point level (figure 17), while the short-time Fourier distribution for density fluctuations within the reflection region illustrates that higher frequencies developed a few periods later (figure 18). This behaviour is similar to the wave–wave interaction

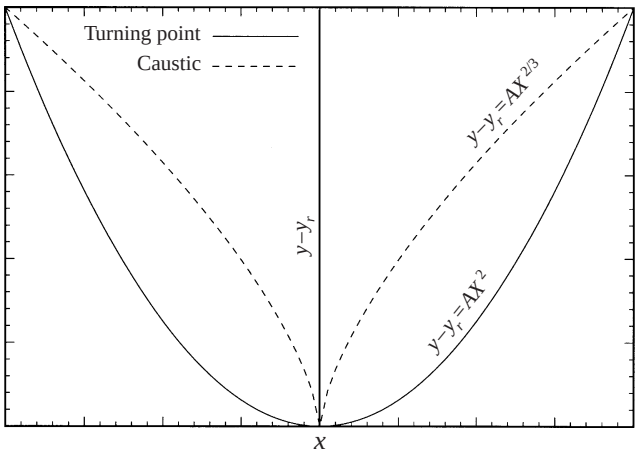

FIGURE 14. Approximated ray paths near the reflection levels. The tangents to the rays are vertical at turning points while they are horizontal at the caustics.

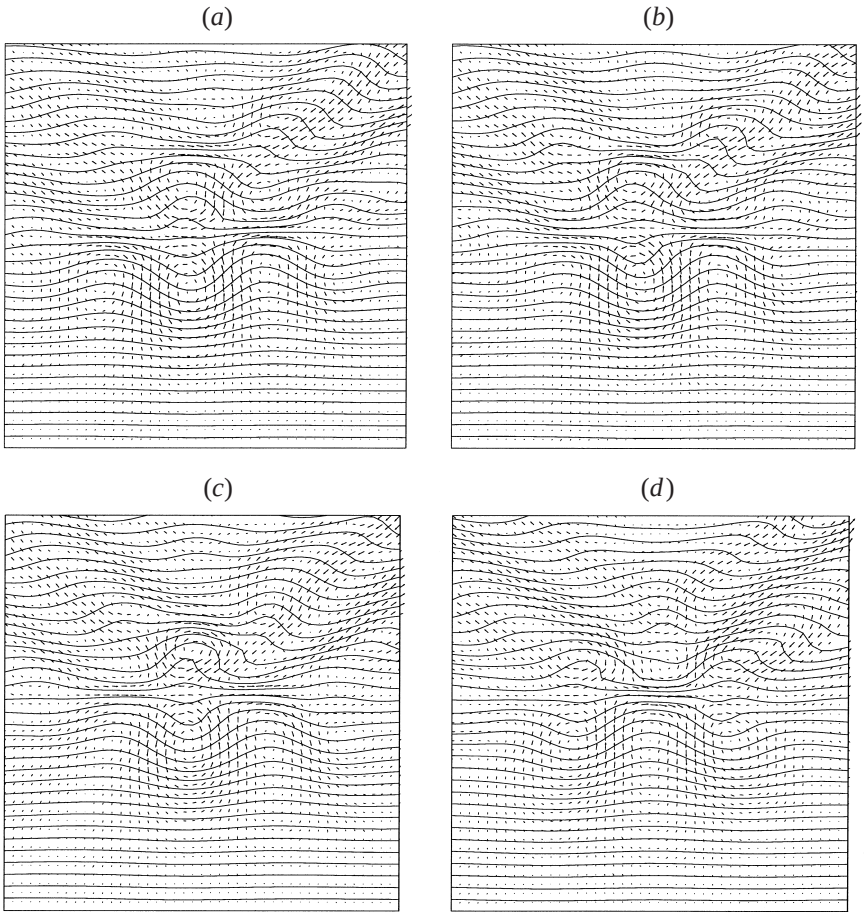

FIGURE 15. Velocity vectors and density contours for $Ke = 0.3$. Times are (*a*) 8, (*b*) 9, (*c*) 10 and (*d*) 10.4. The wave amplitude increases with time above the turning point while it is time independent below the turning point.

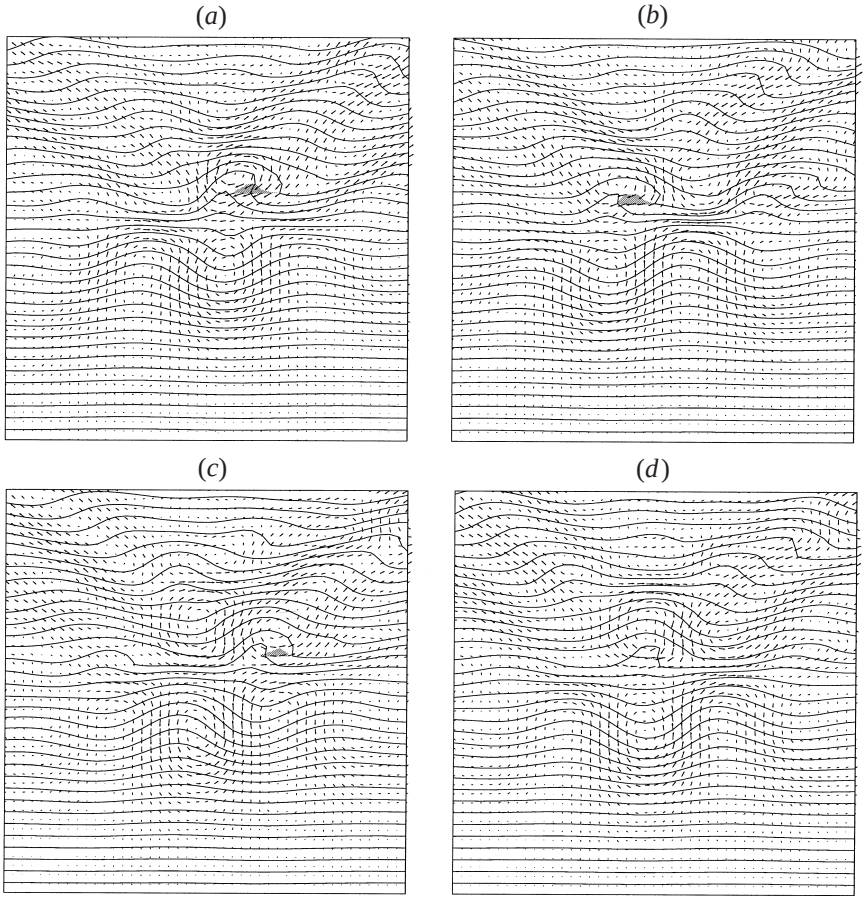

FIGURE 16. Velocity vectors and density contours for $Ke = 0.3$. Shading indicates regions of $Ri_l \leqslant 1/4$. Times are (*a*) 10.8, (*b*) 11.2, (*c*) 11.6 and (*d*) 12. The overturning at the turning point can occur through nonlinear wave–wave–shear interaction.

mechanism discussed in Javam *et al.* (2000). As the wave approached the turning point, part of the energy was transmitted, another portion was reflected, and the remainder was transferred to the higher harmonics. The frequencies of the higher modes were greater than the local buoyancy frequency, thus they could not propagate out of the interaction region. The trapped energy increased the wave amplitude, but this growth of the amplitude was limited by the overturning of the waves due to nonlinearity.

It is important to recognize that the breaking of internal waves at a turning point was due to a different mechanism to that of the breaking at a caustic. With caustic reflection, a triad interaction was formed and provided an energy source for lower modes. However, at the turning point, energy was transferred to trapped higher evanescent modes, similar to what was observed when two symmetric internal wave beams intersect.

3.3. *Critical layer absorption*

The computations for this part of study were carried out under similar conditions to those of the previous simulations. Figure 13 gives velocity vector plots for the

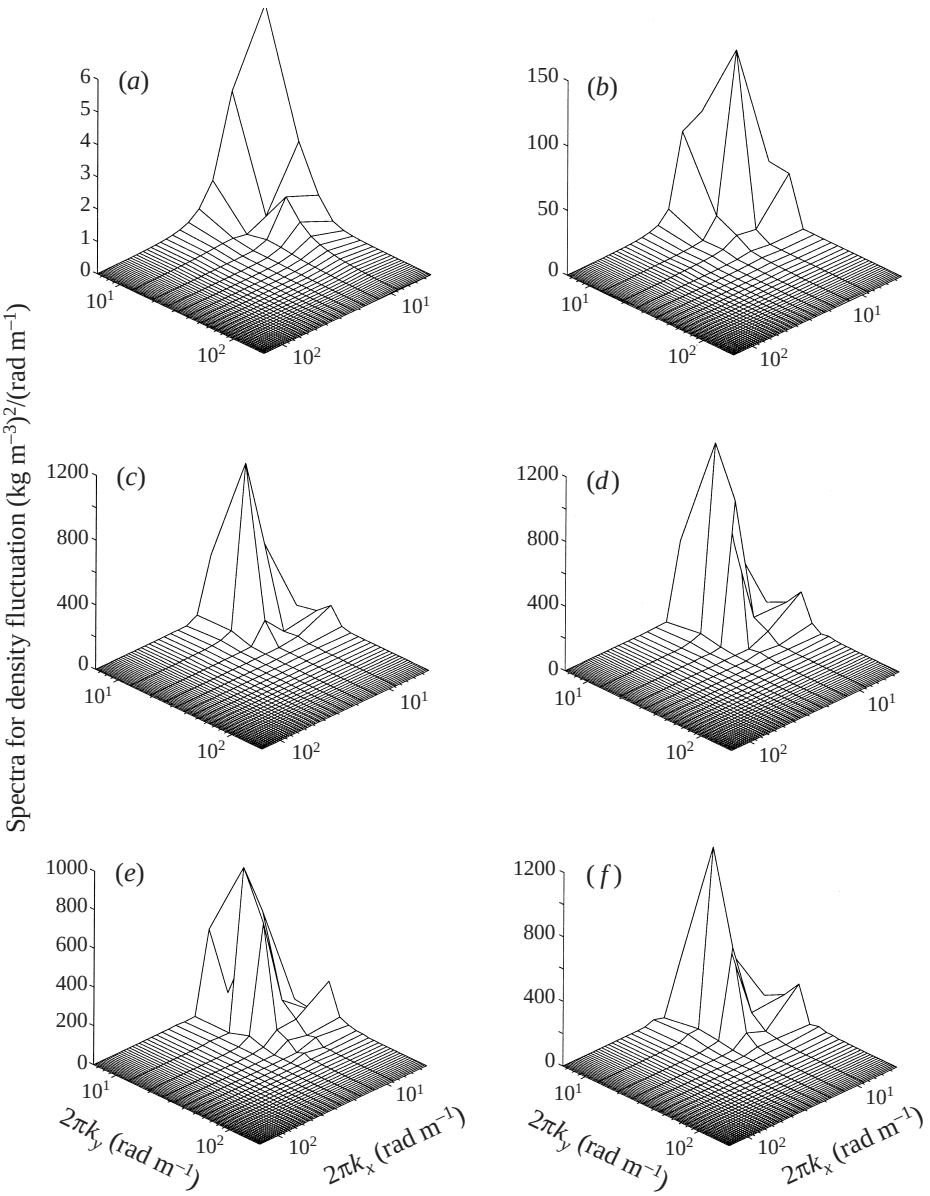

FIGURE 17. Two-dimensional wavenumber spectrum for the reflection region. Times are (*a*) 2, (*b*) 4, (*c*) 6, (*d*) 8, (*e*) 11 and (*f*) 12. Smaller scales are formed as soon as the incident waves reach the turning point.

simulated cases with $Ke = 0.1, 0.2$ and 0.3. It can be seen in this figure that, as the ray approached the critical layer, the horizontal wavenumber became much smaller than the vertical wavenumber and the group velocity became essentially horizontal. The incident wave energy was able to propagate through the critical level for the weakly nonlinear case ($Ke = 0.1$, figure 13*a*) while at higher Keulegan numbers ($Ke > 0.1$, figures 13*b* and 13*c*), the critical layer presented an impenetrable barrier.

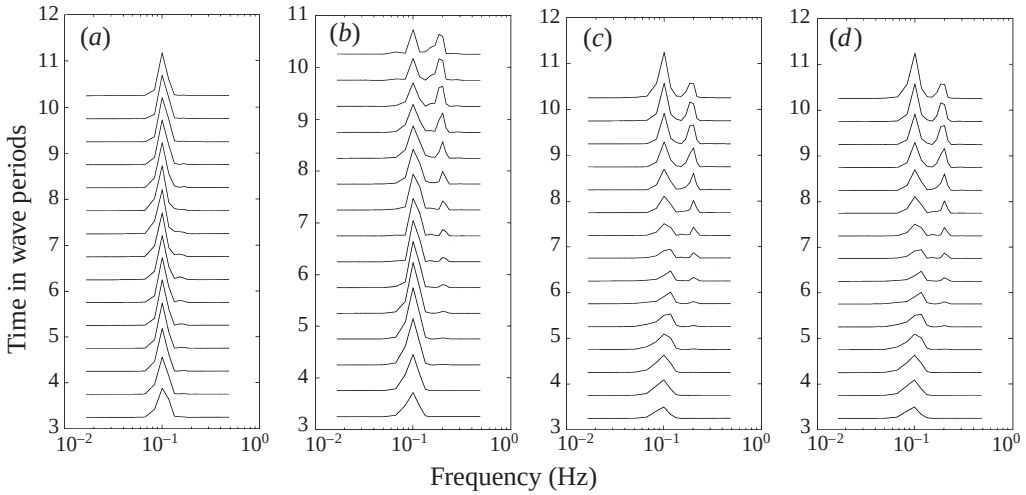

FIGURE 18. Short-time Fourier distribution for density fluctuations for $Ke = 0.3$. Locations are: (*a*) within the incoming ray and (*b–d*) within the interaction region. The wave energy is transferred to higher modes through nonlinear wave–wave interaction in a shear.

The vertical velocity perturbation of the incident wave packet is shown in figure 19. The increase of amplitude with time and the evolution towards smaller vertical scales are evident from this figure, as predicted by linear theory (Fritts 1982). The two-dimensional wavenumber spectrum for density perturbations within the interaction region also shows the production of secondary waves.

Figure 20 contains plots of the horizontal mean velocity and local velocity fluctuations for these three cases at $T = 5$ and $T = 10$ in the interaction region at $x = 19.2\pi$. Dashed and solid lines in this figure indicate local horizontal and mean velocities, respectively. The mean flow near the critical level was accelerated by the transfer of energy from the wave to mean flow. In the higher Keulegan number cases, a smaller proportion of the wave energy reached the critical level. For the case $Ke = 0.1$, the entire wave packet was embedded in the shear and more wave–shear interaction was involved. This resulted in more wave energy being absorbed by the mean flow. Therefore, as the wave packet approached the critical level, part of the wave energy was transferred to the mean flow; this portion of the energy decreased with increasing Keulegan number. The region below the critical level was almost devoid of any wave motion for $Ke > 0.1$, as seen earlier in figure 13, indicating that the degree of wave transmission through the critical level was negligible. There was also no obvious evidence of wave reflection or harmonic generation at the critical level (figure 13). Therefore, the remaining energy may be assumed to be trapped in a region near the critical level.

Density contour plots for the case $Ke = 0.2$ are shown in figure 21. As a wave packet approached the critical level, the phase lines curved because of the decreasing wavelength at the front of the packet. The shrinking vertical scale reduced the vertical group velocity and increased the wave energy density. The wave amplitude became significantly larger, as the wave approached the critical level, only to be damped close to the critical level where the amplitude diminished to zero. Within the region where the wave energy was trapped and the amplitude was amplified, there appeared to be some asymmetry in the horizontal direction, with waves of a considerably steeper

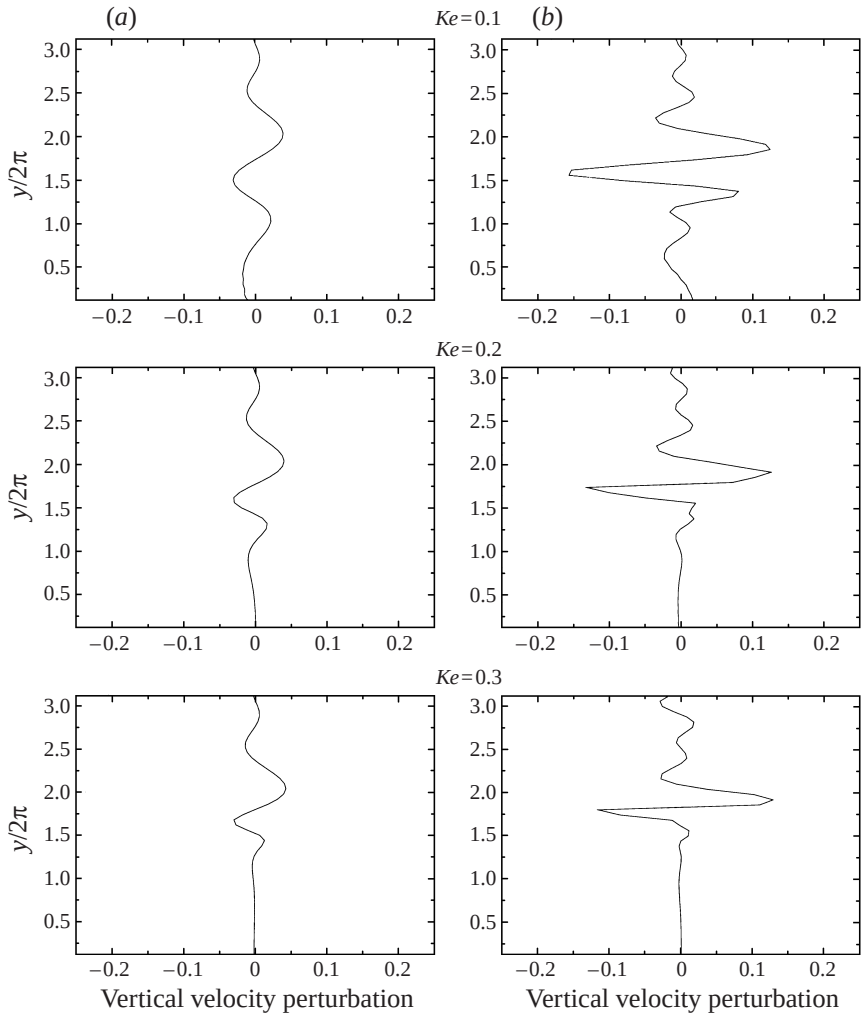

FIGURE 19. The vertical velocity perturbation at $T = 4$ (*a*) and $T = 7$ (*b*) in the absorption region at $x = 19.2\pi$. Keulegan numbers are 0.1, 0.2, and 0.3 (top to bottom). Note the evolution toward smaller vertical scales.

slope occurring on the forward face of the wave followed by more gradual slopes on the rear of the wave. In the neighbourhood of the critical level the flow exhibited small regions of unstable density gradients. These waves, however, retained their basic structure with no evidence of any instability.

The case of $Ke = 0.3$ is an example of a wave–shear interaction where instability was observed near the critical level (figure 22). The waves shown in this figure exhibited the same energy trapping above the critical level as was seen in the previous simulation (figure 21). Similarly, the tendency for wave amplitude to grow as the waves approached the critical level is also seen in this figure. The overturning was the mechanism responsible for limiting the growth of the wave amplitude which occurred at a time of about $T = 7$.

Density and vorticity contour plots (figure 23) show that the strong shear regions

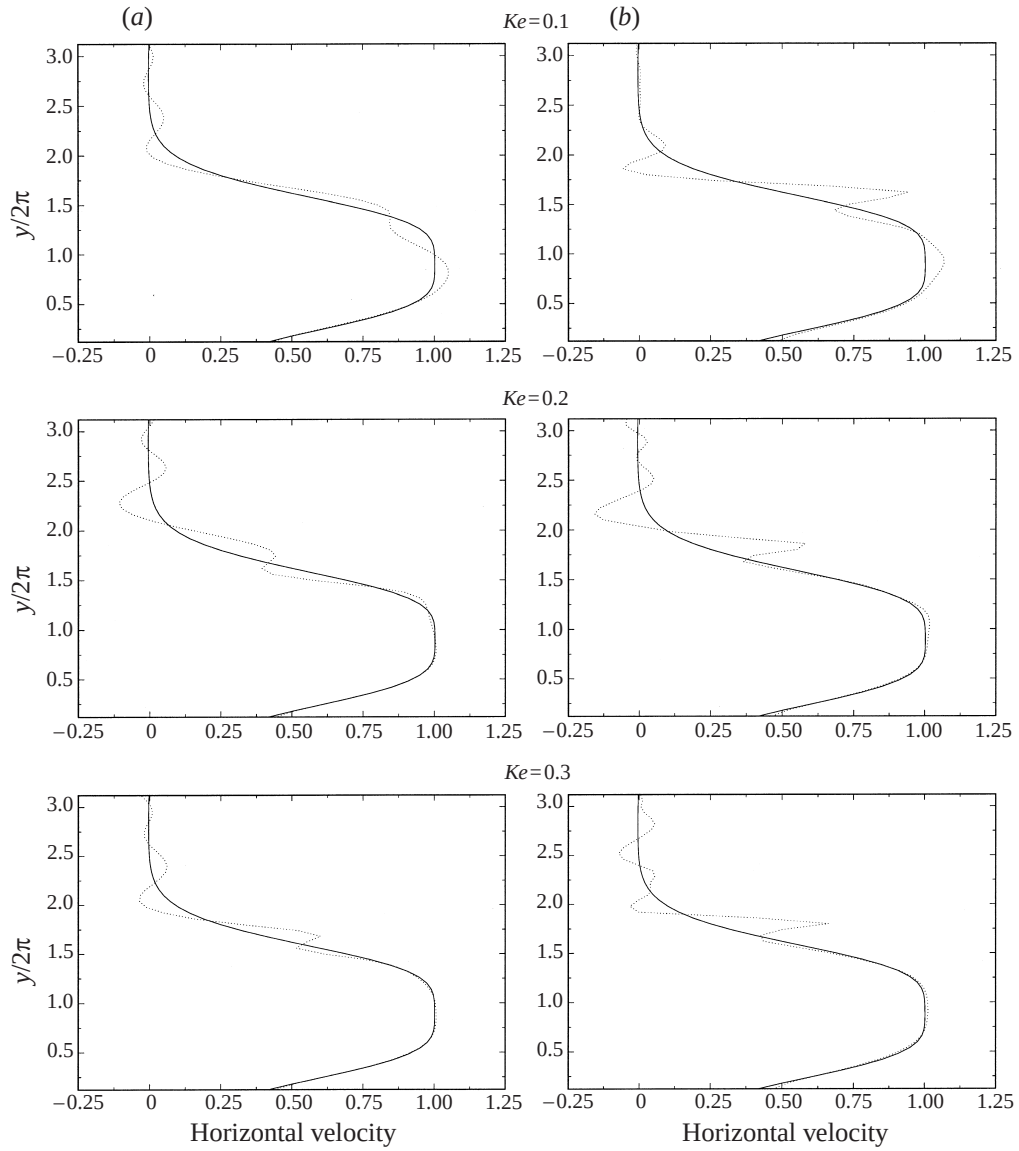

FIGURE 20. Mean and local horizontal velocities at $T = 5$ (a) and $T = 10$ (b) in the absorption region at $x = 19.2\pi$. Keulegan numbers are 0.1, 0.2, and 0.3 (top to bottom). Dashed and solid lines indicate local horizontal and mean velocities respectively. At high Keulegan numbers only a small portion of the wave packet reaches the critical level and turning point.

corresponded to areas where $Ri_l < 1/4$ (indicated by shading) and there was little change in the vorticity field in the unstable regions over time. This means that the density and velocity profiles were in phase and shear instability was possible. Therefore, as the waves propagated towards the critical level, the wave energy was trapped in a region above the critical level and nonlinear wave–shear interaction initiated the instability in this region.

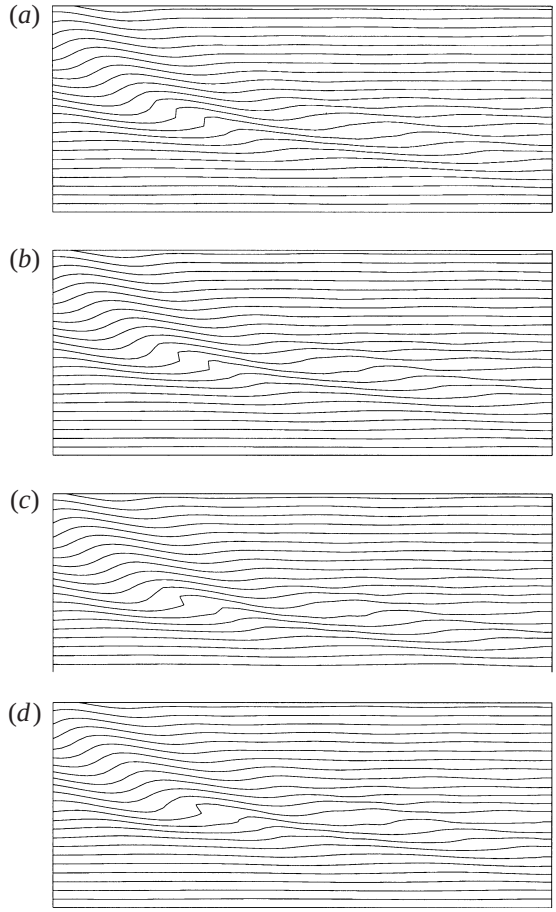

FIGURE 21. The density contour plots for $Ke = 0.2$, times are: (*a*) 9, (*b*) 10, (*c*) 11, and (*e*) 12. Small regions with an unstable density gradient are developed. There is, however, no evidence of any instability.

4. Conclusion

A numerical model has been used to examine internal wave overturning associated with nonlinear reflections. The main conclusions of the study for the case of caustic reflections are as follows. (i) A triad resonant interaction was formed within the reflection region which produced the energy source for lower modes. (ii) Local overturning occurred when the wave amplitude became large. (iii) Overturning appeared to be due to the horizontal advection of density and the results were consistent with the overturning mechanism of Orlanski & Bryan (1969). (iv) One of the excited waves penetrated the caustic level and propagated downwards leading to the possibility of a second reflection below the first.

At a turning point it was found that the mechanism of instability was similar to that of symmetric wave–wave interaction and was totally different to that found at caustic reflections; wave energy was transferred to higher modes through nonlinear wave–wave interactions in a shear. Waves with higher harmonics were trapped in the interaction region as their frequencies were smaller than the local buoyancy frequency.

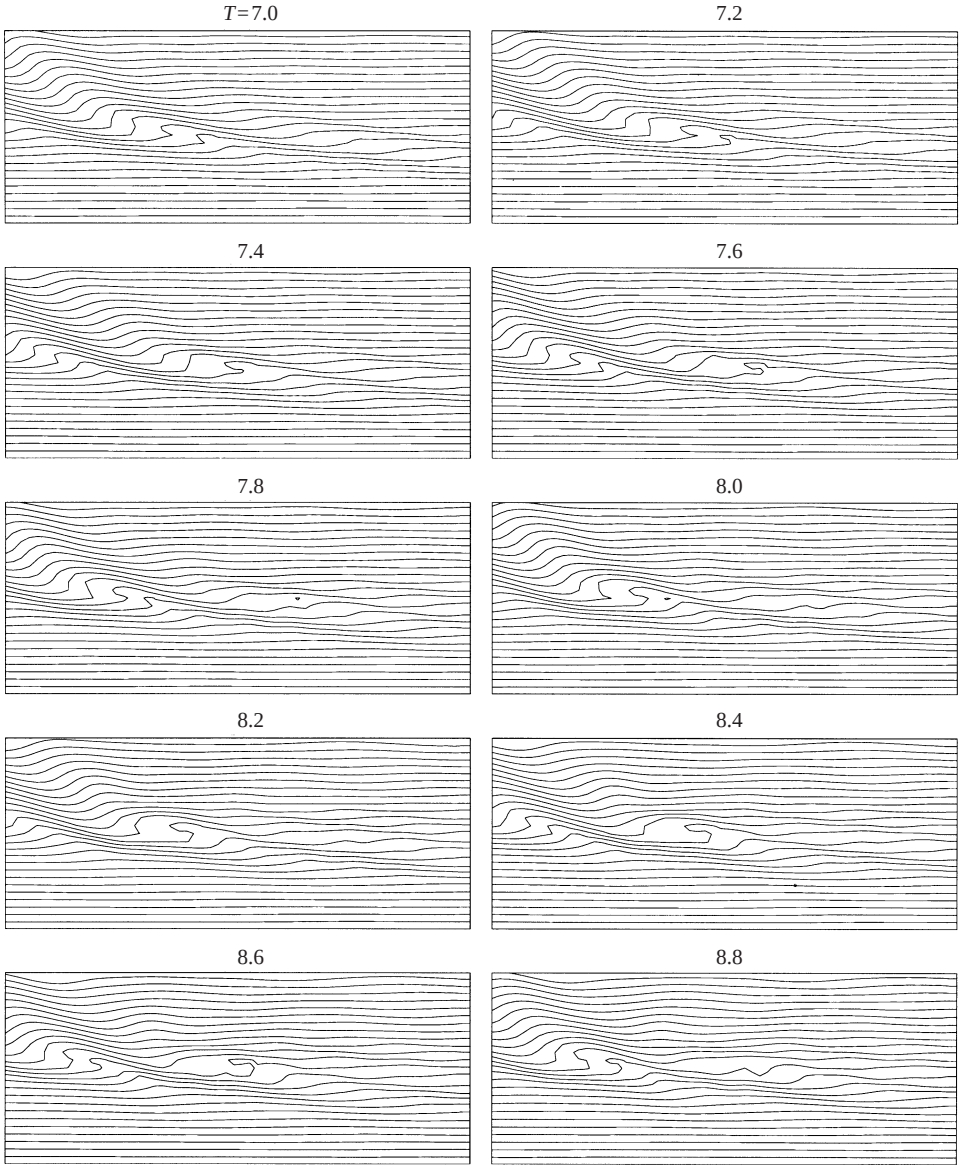

FIGURE 22. Density contour plots for $Ke = 0.3$. Shear instability is observed.

The trapped energy increased the wave amplitude until the waves overturned due to nonlinearity.

By contrast as waves approached a critical level, part of their energy was transferred to the mean flow accelerating the background mean current. The remainder was trapped in a region near the critical level. At low Keulegan numbers most of the wave energy was transferred to the mean flow, so that overturning was not evident. As the Keulegan number increased the critical level became an impenetrable barrier to the incoming waves and more energy was trapped in the region near the critical level. Internal wave overturning followed due to nonlinear wave–mean flow interaction. The results suggest that the critical layer instability was of a shear instability nature.

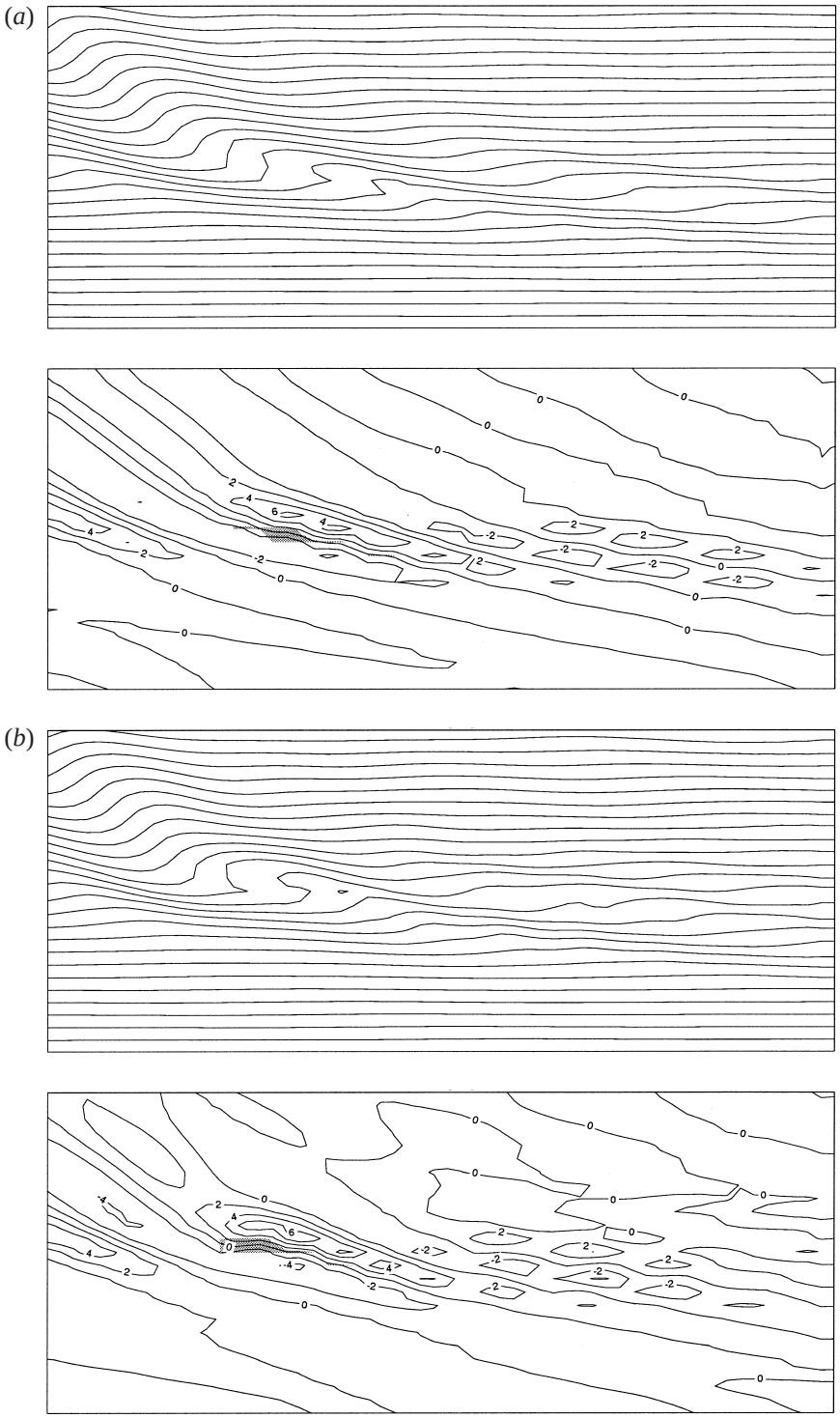

FIGURE 23 (*a, b*). For caption see next page.

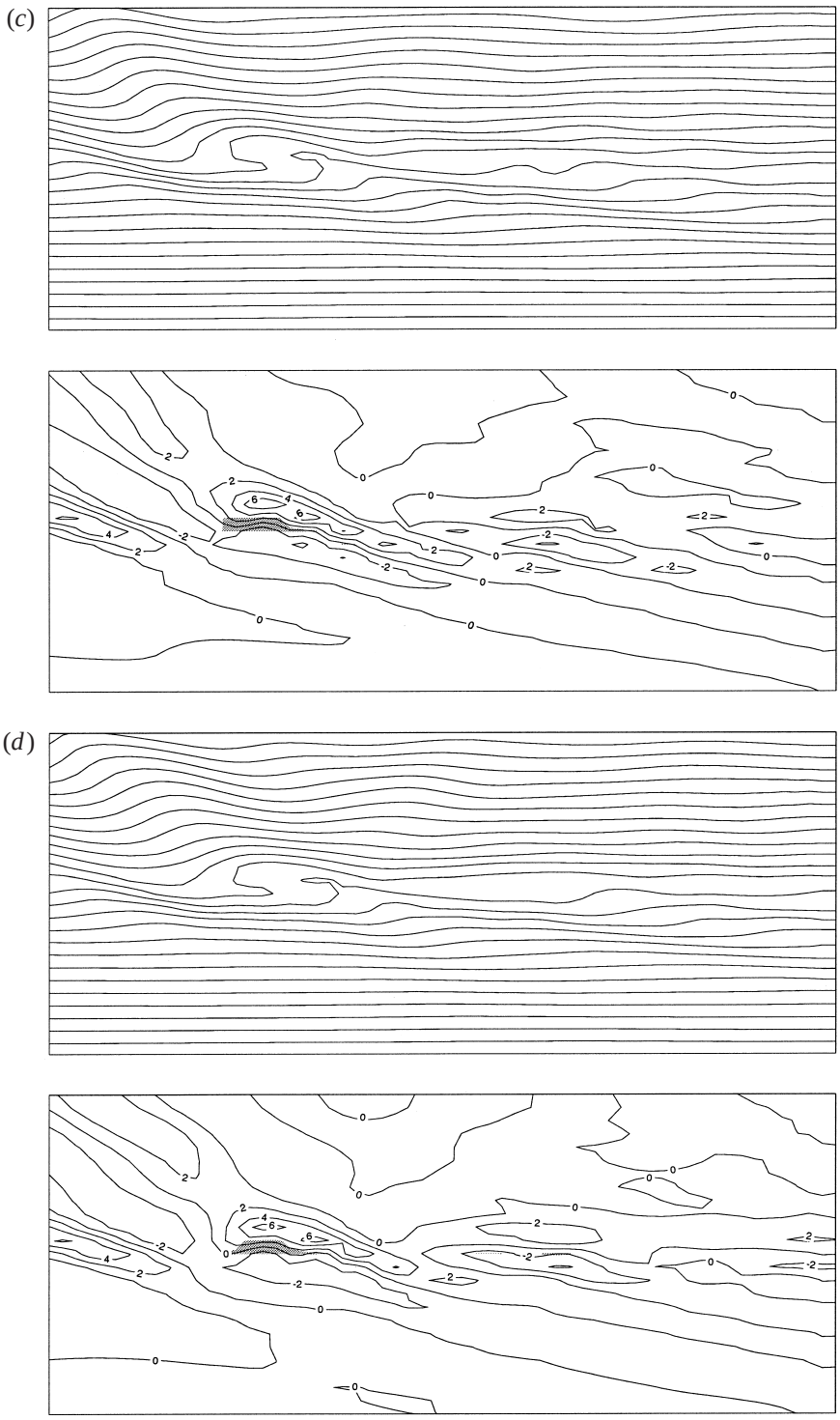

FIGURE 23. Density and vorticity contour plots for $Ke = 0.3$, shading indicates the regions of $Ri_l < 1/4$. The strong shear regions correspond to $Ri_l < 1/4$. (*a*) $T = 7$, (*b*) $T = 8$, (*c*) $T = 9$, (*d*) $T = 10$.

The analysis described above was a part of the first author's PhD study at the Department of Environmental Engineering, The University of Western Australia. Extensive computer resources were provided by the Centre for Environmental Fluid Dynamics (CEFD). The first author wishes to thank the Ministry of Jihade Sazandegi for providing a Scholarship and the CEFD for additional financial support.

REFERENCES

Armfield, S. W. 1994 Ellipticity, accuracy and convergence of the discrete Navier–Stokes equations. *J. Comput. Phys. Fluids* **114**, 176–184.

Booker, J. R. & Bretherton, F. P. 1967 The critical layer for internal gravity waves in a shear flow. *J. Fluid Mech.* **27**, 513–539.

Bouruet-Aubertot, P., Sommeria, J. & Staquet, C. 1995 Breaking of standing internal gravity waves through two-dimensional instabilities. *J. Fluid Mech.* **285**, 265–301.

Bretherton, F. P. 1966 The propagation of groups of internal gravity waves in a shear flow. *Q. J. R. Met. Soc.* **92**, 466–480.

Bretherton, F. P. 1969 Momentum transport by gravity waves. *Q. J. R. Met. Soc.* **16**, 1625–1635.

Brown, S. N. & Stewartson, K. 1980 On the nonlinear reflection of a gravity wave at a critical level. *J. Fluid Mech.* **100**, 577–595.

Davis, R. E. & Acrivos, A. 1967 Solitary internal waves in deep water. *J. Fluid Mech.* **29**, 593–607.

Delisi, D. P. & Orlanski, I. 1975 On the role of density jumps in the reflection and breaking of internal gravity waves. *J. Fluid Mech.* **69**, 445–464.

Drazin, P. G. 1977 On the instability of an internal gravity wave. *Proc. R. Soc. Lond.* A **356**, 411–432.

Eliassen, A. & Palm, E. 1961 On the transfer of energy in stationary mountain waves. *Geophys. Publ.* **22**, 1–23.

Fritts, D. C. 1982 The Transient critical-level interaction in a Boussinesq fluid. *J. Geophys. Res.* **87**, 7997–8016.

Gregg, M. C., D'Asaro, E. A., Shay, T. J. & Larson, N. 1986 Observations of persistent mixing and near-inertial waves. *J. Phys. Oceanogr.* **16**, 856–885.

Hartman, R. J. 1975 Wave propagation in a stratified shear flow. *J. Fluid Mech.* **71**, 89–104.

Javam, A., Armfield, S. W. & Imberger, J. 2000 Numerical study of internal wave–wave interaction in a stratified fluid. *J. Fluid Mech.* **415**, 65–87.

Koop, C. G. 1981 A preliminary investigation of the interaction of internal gravity waves with a steady shearing motion. *J. Fluid Mech.* **113**, 347–386.

Koop, C. G. & McGee, B. 1986 Measurements of internal gravity waves in a continuously stratified shear flow. *J. Fluid Mech.* **172**, 453–480.

Lighthill, M. J. 1978 *Waves in Fluids*. Cambridge University Press.

Lin, C. L., Ferziger, J. H., Kossef, J. R. & Monismith, S. G. 1993 Simulation and stability of two-dimensional internal gravity waves in a stratified shear flow. *Dyn. Atmos. Oceans* **19**, 325–366.

Liu, R. 1989 A numerical and analytical study of internal waves in stratified fluids. PhD thesis, University of Manchester.

Liu, R., Nicolaou, D. & Stevenson, T. N. 1990 Waves from an oscillatory disturbance in a stratified shear flow. *J. Fluid Mech.* **219**, 609–619.

McEwan, A. D. & Robinson, R. M. 1975 Parametric instability of internal gravity waves. *J. Fluid. Mech.* **67**, 667–687.

Marmorino, G. O., Rosenblum, L. J. & Trump, C. L. 1987 Fine-scale temperature variability: The influence of near-inertial waves. *J. Geophys. Res.* **92**, 13049–13062.

Miles, J. W. 1961 On the instability of heterogeneous shear flows. *J. Fluid Mech.* **10**, 496–508.

Miranda, P. M. A. & James, I. N. 1992 Non-linear three-dimensional effects on gravity-wave drag. Splitting flow and breaking waves. *Q. J. R. Met. Soc.* **118**, 1057–1082.

Mowbray, D. E. & Rarity, B. S. H. 1967 A theoretical and experimental investigation of the phase configuration of internal waves of small amplitude in a density stratified fluid. *J. Fluid Mech.* **28**, 1–16.

MUNK, W. H. 1980 Internal waves and small scale process. In *Evolution of Physical Oceanography* (ed. B. A. Warren & C. Wunsch), pp. 264–291. Massachusetts Institute of Technology Press.

NICOLAOU, D., LIU, R. & STEVENSON, T. N. 1993 The evolution of thermocline waves from an oscillatory disturbance. *J. Fluid Mech.* **254**, 401–416.

ORLANSKI, I. & BRYAN, K. 1969 Formation of the thermocline step structure by large-amplitude internal gravity waves. *J. Geophys. Res.* **74**, 6975–6983.

PHILLIPS, O. M. 1977 *The Dynamics of the Upper Ocean*, 2nd Edn. Cambridge University Press.

TEOH, S. G., IVEY, G. N. & IMBERGER, J. 1997 Experimental study of two intersecting internal waves. *J. Fluid Mech.* **336**, 91–122.

THORPE, S. A. 1968*a* On standing internal gravity waves of finite amplitude. *J. Fluid Mech.* **32**, 489–528.

THORPE, S. A. 1968*b* A method of producing a shear flow in a stratified fluid. *J. Fluid Mech.* **32**, 693–704.

THORPE, S. A. 1973 Turbulence in stably stratified fluids: a review of laboratory experiments. *Boundary-layer Met.* **5**, 95–119.

THORPE, S. A. 1978 On the shape and breaking of finite-amplitude internal gravity waves in a shear flow. *J. Fluid Mech.* **85**, 7–31.

THORPE, S. A. 1981 An experimental study of critical layers. *J. Fluid Mech.* **103**, 321–344.

THORPE, S. A. 1994 Statically unstable layers produced by overturning internal gravity waves. *J. Fluid Mech.* **260**, 333–350.

WINTERS, K. B. & D'ASARO, E. A. 1989 Two-dimensional instability of finite amplitude internal gravity wave packets near a critical level. *J. Geophys. Res.* **94**, 12709–12719.

WOODS, J. D. 1968 Wave-induced shear instability in the summer thermocline. *J. Fluid Mech.* **32**, 791–800.